



**HAL**  
open science

## Ganymede's atmosphere as constrained by HST/STIS observations

François Leblanc, L. Roth, Jean-Yves Chaufray, Ronan Modolo, M. Galand, Nickolay Ivchenko, Gianluca Carnielli, Claire Baskevitch, A. Oza, Elisabeth Werner

► **To cite this version:**

François Leblanc, L. Roth, Jean-Yves Chaufray, Ronan Modolo, M. Galand, et al.. Ganymede's atmosphere as constrained by HST/STIS observations. *Icarus*, 2023, 399, pp.115557. 10.1016/j.icarus.2023.115557 . insu-04056918

**HAL Id: insu-04056918**

**<https://insu.hal.science/insu-04056918>**

Submitted on 5 Jul 2023

**HAL** is a multi-disciplinary open access archive for the deposit and dissemination of scientific research documents, whether they are published or not. The documents may come from teaching and research institutions in France or abroad, or from public or private research centers.

L'archive ouverte pluridisciplinaire **HAL**, est destinée au dépôt et à la diffusion de documents scientifiques de niveau recherche, publiés ou non, émanant des établissements d'enseignement et de recherche français ou étrangers, des laboratoires publics ou privés.

1 **Ganymede's atmosphere as constrained by HST/STIS observations**

2

3 F. Leblanc<sup>1</sup>, Roth L.<sup>2</sup>, Chaufray J.Y.<sup>1</sup>, R. Modolo<sup>1</sup>, M. Galand<sup>3</sup>, N. Ivchenko<sup>2</sup>, G.

4 Carnielli<sup>3</sup>, C. Baskevitch<sup>1</sup>, A. Oza<sup>4</sup> and A.L.E. Werner<sup>1,5</sup>

5

6 <sup>1</sup> LATMOS/CNRS, Sorbonne Université, UVSQ, Paris, France

7 <sup>2</sup> Space and Plasma Physics, KTH Royal Institute of Technology, Stockholm, Sweden

8 <sup>3</sup> Department of Physics, Imperial College London, London, UK

9 <sup>4</sup> Jet Propulsion Laboratory, California Institute of Technology, Pasadena, USA

10 <sup>5</sup> Now at Swedish Institute of Space Physics, Uppsala, Sweden

11

12

13 **Abstract**

14 A new analysis of aurora observations of Ganymede's atmosphere on the orbital leading and trailing  
15 hemispheres has been recently published by Roth et al. (2021), suggesting that water is its main  
16 constituent near noon. Here, we present two additional aurora observations of Ganymede's sub-Jovian  
17 and anti-Jovian hemispheres, which suggest a modulation of the atmospheric H<sub>2</sub>O/O<sub>2</sub> ratio on the  
18 moon's orbital period, and analyze the orbital evolution of the atmosphere. For this, we propose a  
19 reconstruction of aurora observations based on a physical modelling of the exosphere taking into  
20 account its orbital variability (the Exospheric Global Model; Leblanc et al. 2017). The solution described  
21 in this paper agrees with Roth et al. (2021) that Ganymede's exosphere should be dominantly  
22 composed of water molecules. From Ganymede's position when its leading hemisphere is illuminated  
23 to when it is its trailing hemisphere, the column density of O<sub>2</sub> may vary between  $4.3 \times 10^{14}$  and  $3.6 \times 10^{14}$   
24 cm<sup>-2</sup> whereas the H<sub>2</sub>O column density should vary between  $5.6 \times 10^{14}$  and  $1.3 \times 10^{15}$  cm<sup>-2</sup>. The water  
25 content of Ganymede's atmosphere is essentially constrained by its sublimation rate whereas the O<sub>2</sub>  
26 component of Ganymede's atmosphere is controlled by the radiolytic yield. The other species,  
27 products of the water molecules, vary in a more complex way depending on their sources, either as  
28 ejecta from the surface and/or as product of the dissociation of the other atmospheric constituents.  
29 Electron impact on H<sub>2</sub>O and H<sub>2</sub> molecules is shown to likely produce H Lyman-alpha emissions close to  
30 Ganymede, in addition to the observed extended Lyman-alpha corona from H resonant scattering. All  
31 these conclusions being highly dependent on our capability to accurately model the origins of the  
32 observed Ganymede auroral emissions, modelling these emissions remains poorly constrained without  
33 an accurate knowledge of the Jovian magnetospheric and Ganymede ionospheric electron  
34 populations.

## 35 I Introduction

36 As summarized in Roth et al. (2022), only very few direct observations of Ganymede's atmosphere  
37 have been realized so far. The very first evidence of Ganymede's atmosphere was obtained by Galileo  
38 FUV instrument in 1996 (Barth et al. 1997) and revealed an extended atmosphere of H atoms, an  
39 observation later confirmed by the Space Telescope Imaging Spectrograph of the Hubble Space  
40 Telescope (HST/STIS; Feldman et al. 2000; Alday et al. 2017). Alday et al. (2017) concluded that the  
41 Lyman  $\alpha$  emission brightness does not vary along Ganymede's orbit with an average corona emission  
42 intensity of  $\sim 320$  R corresponding to a column density of  $1.55 \pm 1.2 \times 10^{12}$  H/cm<sup>2</sup> if only produced by  
43 resonant scattering. Recent HST/STIS observations of Ganymede in transit (Roth et al. 2023) found  
44 weak but widely extended absorption around the moon, confirming the H corona profile and densities  
45 derived earlier. In 1996, the Goddard High Resolution Spectrograph of the Hubble Space Telescope  
46 (HST/GHRS) obtained the first evidence of two other emission lines at 130.4 and 135.6 nm from  
47 Ganymede's atmosphere (Hall et al. 1998). The ratio of these two emissions strongly suggested that  
48 these observed emissions were probably due to electron impact on O<sub>2</sub> molecules. Moreover, the first  
49 images of these emission lines obtained by HST/STIS clearly showed that the 135.6 nm was confined  
50 in the polar regions (Hall et al. 1998) and even roughly collocated to the open-closed field line boundary  
51 (OCFB) of Ganymede magnetosphere (McGrath et al. 2013; Molyneux et al. 2018). The auroral nature  
52 of these two emissions implies that their brightnesses depend essentially on three parameters: the  
53 column density and composition of the neutral atmosphere and the energy flux distribution of the  
54 electrons. When supposing that the observed emission was only produced by electron impact on O<sub>2</sub>,  
55 without a knowledge of the electron distribution in these regions, the column density of O<sub>2</sub>/cm<sup>2</sup> could  
56 not be estimated very accurately and was inferred to be between  $10^{14}$  to  $10^{15}$  O<sub>2</sub>/cm<sup>2</sup> (Hall et al. 1998;  
57 Molyneux et al. 2018). No observation constraining the H<sub>2</sub>O, OH and H<sub>2</sub> exosphere of Ganymede has  
58 been obtained up to Roth et al. (2021), whereas the oxygen atomic species was tentatively identified  
59 (Molyneux et al. 1998; Roth et al. 2021).

60

61 Considering the relatively limited number of observations and the difficulty to realize new ones,  
62 modelling Ganymede's atmosphere remains presently our best approach to get an idea on how this  
63 atmosphere might be spatially organized and temporarily variable. This atmosphere is thought to be  
64 essentially composed of H<sub>2</sub>O, O<sub>2</sub> and their products. H<sub>2</sub>O is essentially produced by sublimation near  
65 the subsolar point, which according to Marconi (2007), Shematovitch (2016) and Leblanc et al. (2017)  
66 leads to a partially surface bounded exosphere in reference to the Moon exosphere (Stern 1999). But  
67 H<sub>2</sub>O can also be produced by the sputtering of Ganymede icy surface (Cassidy et al. 2013) at high  
68 latitudes.

69 Our ability to model Ganymede's atmosphere depends therefore on several parameters:

70 - the surface temperature and composition (Spencer et al. 1989; Leblanc et al. 2017),

71 - the spatial dependency of the ion bombardment of the surface by the Jovian particles (Plainaki et al.  
72 2020a, b; Vorburger et al. 2022) but also by ions produced locally in Ganymede's neutral atmosphere  
73 (Carnielli et al. 2020b),

74 - the ejection rate induced by the sputtering (Cooper et al. 2001; Turc et al. 2014; Plainaki et al. 2015;  
75 2020a, b and Carnielli et al. 2020a, b) and by sublimation (Johnson et al. 1989; Fray and Schmitt 2009;  
76 Leblanc et al. 2017; Vorburger et al. 2022),

77 - the losses by photon and electron ionization and dissociation, as well as by reabsorption at the surface  
78 and by neutral and ion escape,

79 - the orbital variability of all these parameters (Plainaki et al. 2015; Leblanc et al. 2017).

80 Recently, Roth et al. (2021) proposed an original analysis of new and old HST/STIS observations  
81 obtained at two different orbital positions of Ganymede. These authors suggested that the radial  
82 distribution of the 130.4 nm and 135.6 nm emission lines brightness was consistent with the existence  
83 of a dominant H<sub>2</sub>O atmospheric component and with its predicted orbital variability. Based on a simple  
84 symmetric model of the atmosphere, Roth et al. (2021) concluded that Ganymede's atmosphere water

85 column density peaks at a value of  $6 \times 10^{15}$  H<sub>2</sub>O/cm<sup>2</sup> near the center of the visible disk when the trailing  
86 hemisphere is illuminated, a value which decreases to  $1 \times 10^{15}$  H<sub>2</sub>O/cm<sup>2</sup> when the leading hemisphere  
87 of Ganymede is illuminated.

88 In the following, we present a detailed comparison between these observations and the results of  
89 simulation performed with Exospheric Global Model, EGM (Leblanc et al. 2017; Oza et al. 2019). In  
90 section II, we briefly describe the set of observations analyzed in this paper, in section III, our model,  
91 whereas in section IV a detailed comparison and discussion of the main lessons from such a comparison  
92 are provided. Section V summarizes the main conclusions of this work.

93

## 94 **II HST/STIS Observations**

95 Roth et al. (2021) reported the first indirect observation of Ganymede water atmosphere. They used  
96 two sets of images by Hubble's Space Telescope Imaging Spectrograph (HST/STIS) performed at two  
97 positions of Ganymede along its orbit:

98 - at a phase angle of  $98^\circ - 111^\circ$  (2010-11-19, Figure 1 in yellow), that is with the leading hemispheric  
99 side of Ganymede being illuminated,

100 - at a phase angle of  $289^\circ - 300^\circ$  (1998-10-30, Figure 1 in blue), that is with the trailing hemispheric  
101 side of Ganymede being illuminated.

102 In addition, Roth et al. (2021) analyzed spectra taken with HST's Cosmics Origins Spectrograph (COS)  
103 at a phase angle of  $352^\circ - 357^\circ$ , that is just before and partly when Ganymede is in the shadow of  
104 Jupiter. At such phase angle, they reported no significant change in the relative intensity of the two  
105 oxygen lines, 130.4 and 135.6 nm, suggesting that the atomic oxygen atmospheric content should  
106 not exceed  $2 \times 10^{12}$  O/cm<sup>2</sup>. In the following, we will not use the COS spectra in our analysis because  
107 these observations were only used to estimate an upper limit for the exospheric content in atomic  
108 oxygen and do not provide useful spatial information on the emissions.

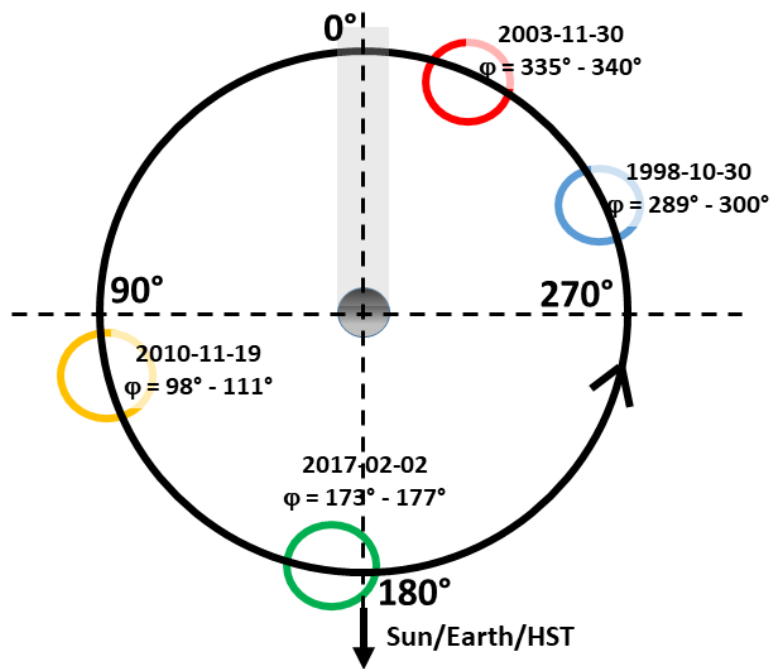
109 To the two sets of HST/STIS observations, we add two other sets of HST/STIS observations obtained  
110 at two complementary positions of Ganymede (Figure 1; Marzok et al. 2022):

- 111 - at a phase angle of  $173\text{-}177^\circ$  obtained with STIS on the 02/02/2017 (Figure 1, in green),
- 112 - at a phase angle of  $335^\circ\text{-}340^\circ$  obtained with STIS on the 11/30/2003 (Figure 1, in red).

113 These two later sets of observations nicely complete the ones described in Roth et al. (2021) even if  
114 obtained with lower signal/noise ratio (Figure 2) and allow us to track the atmospheric orbital  
115 variability. The 135.6 nm images have been published in McGrath et al. (2013) (2003 dataset) and  
116 Marzok et al. (2022) (2017 dataset). For this study, the 130.4 images obtained simultaneously were  
117 analyzed for the first time and are used in addition. The data processing and image analysis of the  
118 new datasets follows the same steps as described in Roth et al. (2021), Roth et al. (2016) and (2014):

- 119 - Earth 130.4 nm Geocorona is taken into account by selecting low-Geocorona exposures when HST  
120 was in Earth's nightside and by monitoring the 130.4 nm background signal as HST moves into Earth's  
121 shadow (Roth et al. 2016). The background induced by the Geocorona, interplanetary medium and  
122 torus emissions is also estimated and subtracted using two regions far from Ganymede disk along the  
123 slit (Roth et al. 2014).
- 124 - Solar reflected light from Ganymede's surface (surface albedo) is subtracted from the observation  
125 using UV daily observations by SORCE/SOLSTICE instrument (McClintock et al. 2005) taking into  
126 account STIS G140L resolution and using a homogeneous bright model disk of Ganymede convolved  
127 with STIS Point Spread Function and adjusted to match the observed surface reflection signal  
128 between 143 and 153 nm. We have tested different phase angle dependencies for the surface  
129 reflection between a uniform disk (as used in Roth et al. 2021) and a Lambertian reflector using the  
130 description from Oren and Nayar (1994). The effects on the resulting emission ratio is less than 10%  
131 and for the presented results we used the simple uniform disk reflectance.

132 From the corrected HST/STIS images, we calculated the radial profiles of the intensity of the 130.4  
 133 and 135.6 nm emissions by integrating its brightness on annulus centred on Ganymede's disk and  
 134 binned in steps of  $0.2 R_G$  for the observations obtained at a phase angle of  $98^\circ$ - $111^\circ$  and  $298^\circ$ - $300^\circ$   
 135 (panels a and d in Figure 2), of  $0.4 R_G$  for a phase angle of  $335^\circ$ - $340^\circ$  (panel b in Figure 2) and of  $0.25$   
 136  $R_G$  for a phase angle of  $173^\circ$ - $177^\circ$  (panel c in Figure 2). The large bin size in panel b is chosen to get  
 137 somewhat lower error bars while still keeping a reasonable number of 4 bins to actually see a radial  
 138 profile trend.

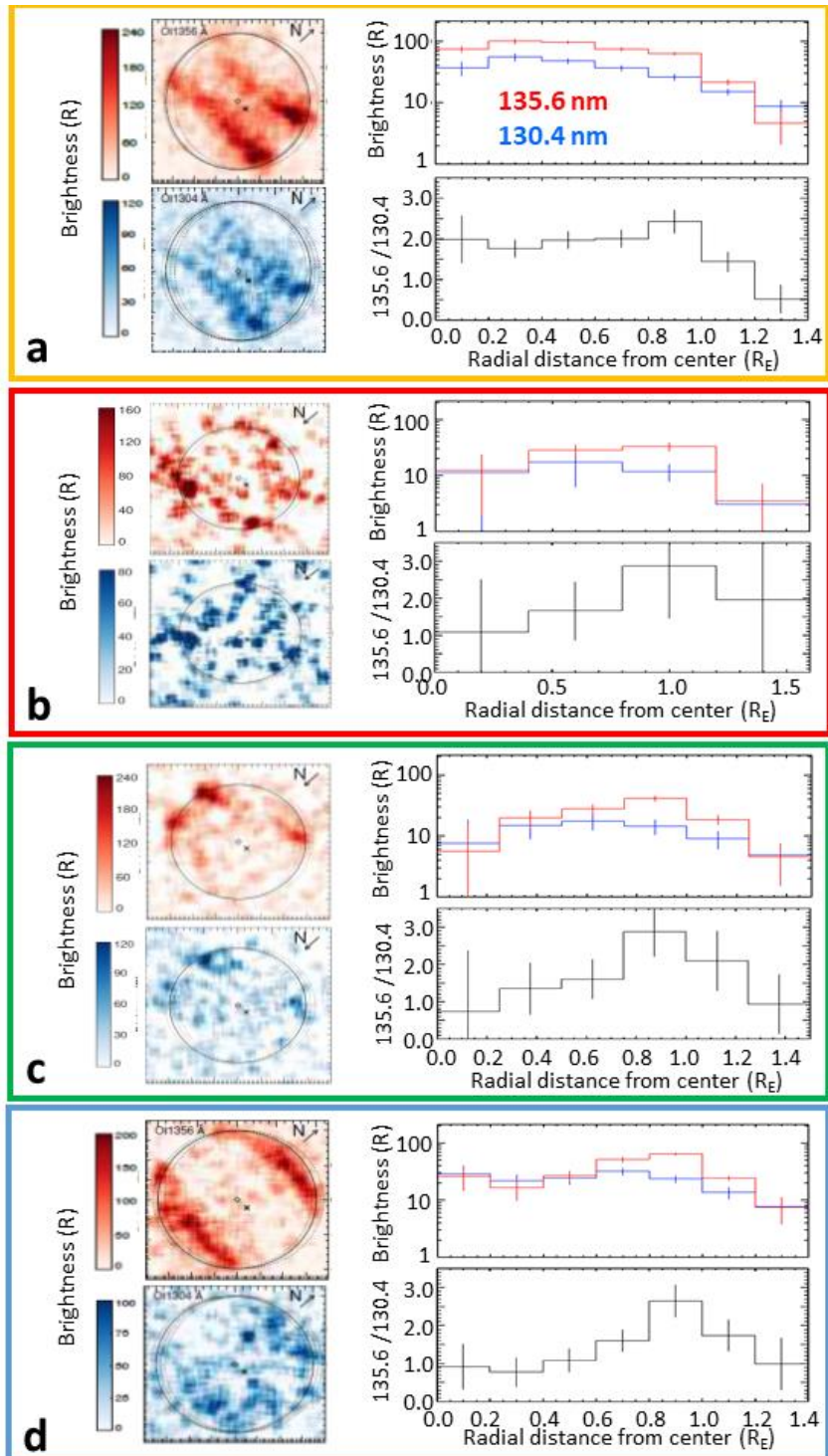


139  
 140 **Figure 1:** Positions of Ganymede during the four sets of observations of HST/STIS used in this paper. We  
 141 also indicated the range of phase angle of each set of observations as well as their date. The caption  
 142 colors of the circle refer to Figures 2 and 6.

143  
 144 Figure 2 provides a view of the four sets of observations used in this paper. At the four orbital positions  
 145 of Ganymede (Figure 1), HST/STIS realized 2D images of the emission brightness intensity of the 130.4  
 146 nm and 135.6 nm emission lines (left panels of each set of observations) from which it was possible to



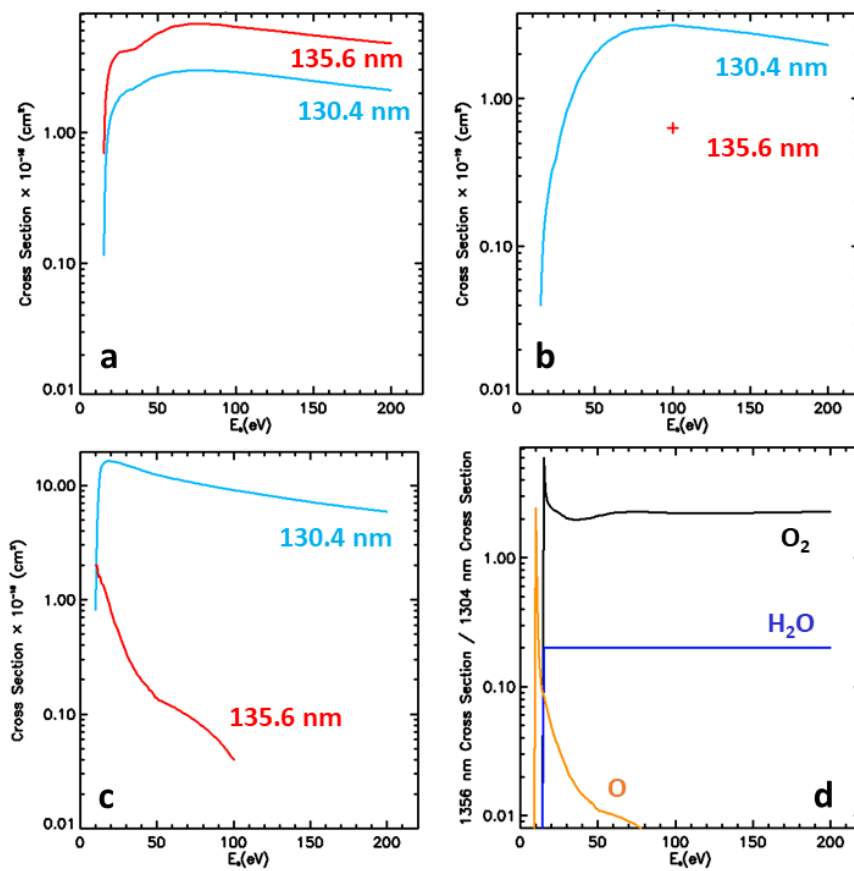
147 extract an average emission intensity profile with respect to the distance from the center of Ganymede  
148 apparent disk (right top panel). We also derived the ratio of these two emissions lines as a function of  
149 the distance from the center (right bottom panels). This ratio is displayed up to  $1.4 R_G$  whereas the 2D  
150 images show pixels up to at least  $1.2 R_G$  (panel d). The observations use a long slit and the images  
151 therefore do not go beyond the left and right edges shown in Figure 2, but above and below the  
152 displayed images. However, because the signal-to-noise ratio of a single pixel is well below 1 at  
153 distances  $> 1.2 R_G$ , we choose not to show those pixels above  $1.2 R_G$  in these 2D images. When the  
154 signal was low, we rather choose to integrate over few pixels to show a significant signal, not  
155 necessarily showing the noisy spatially resolved data. As explained in Roth et al. (2021) and displayed  
156 in Figure 3d, this ratio should be of  $\sim 2.3$  if both emissions are produced by the electron impact on  $O_2$   
157 only. The ratio is close to  $\sim 0.2$  if produced by electron impact on  $H_2O$  and is lower than 0.1 if produced  
158 by electron impact on atomic O (Figure 3d).



159

160 **Figure 2:** Observation of Ganymede's atmospheric emission by HST/STIS. Each panel corresponds to  
 161 one position displayed in Figure 1: a 2010-11-19, phase angle of  $98^{\circ}$ - $111^{\circ}$  (Roth et al. 2021). b: 2003-  
 162 11-30, phase angle of  $335^{\circ}$ - $340^{\circ}$  (McGrath et al. 2013). c: 2017-02-02, phase angle of  $173^{\circ}$  -  $177^{\circ}$ . d:  
 163 1998-10-30, phase angle between  $289^{\circ}$  -  $300^{\circ}$  (Roth et al. 2021). Each panel surrounded by a rectangle  
 164 whose colour corresponds to that used for the circles in Figure 1 is composed of the STIS images of the

165 135.6 nm (red) and 130.4 nm (blue) brightness intensities, of the radial profile from the center of the  
 166 disk up to around half a radius above the limb of the emission brightness intensity at these two  
 167 wavelengths (top right panel in each rectangle where the red solid line corresponds to the 135.6 nm  
 168 emission brightness and the blue solid line to the 130.4 nm emission brightness) and of the ratio of the  
 169 135.6 nm emission intensity divided by the 130.4 nm emission intensity (bottom right panel in each  
 170 rectangle). The North direction in panels b and c (pointing towards the bottom of the figure) is inverted  
 171 with respect to the North direction in panels a and b (pointing towards the top of the figure).



172

173 **Figure 3:** Emission excitation electron impact cross sections. a:  $O_2 + e$  (Kanik et al. 2003). b:  $H_2O + e$   
 174 (Makarov et al. 2004) and only available measurement of the  $H_2O + e$  135.6 nm at 100 eV (Roth et al.  
 175 2021). c:  $O + e$  (Tayal et al. 2016 for 135.6 nm; Johnson et al. 2005 for 130.4 nm). d: ratio of the 135.6  
 176 nm / 130.4 nm emission excitation cross section for  $O_2 + e$  (black line),  $H_2O + e$  (blue line, with the  
 177 assumption that the only measurement at 100 eV is valid on the whole range of electron energy plotted  
 178 here) and  $O + e$  (orange line).

179

180 As displayed in Figure 2, the observed ratio of the 135.6 nm / 130.4 nm emission line brightness varies  
181 between 3.0 and 0.5 and was interpreted as a signature of the mixture of H<sub>2</sub>O or O relative to O<sub>2</sub>. Roth  
182 et al. (2021) also suggested that the contribution to these emission lines from electron impact on  
183 atomic oxygen was negligible on the disk but can explain the observed decrease in the 135.6 nm /  
184 130.4 nm ratio above the limb (at radial distance > 1 R<sub>G</sub> in Figure 2).

185 As shown in Figure 2, the best observations in terms of signal noise ratio were obtained when  
186 Ganymede was at a phase angle of 98° - 111° (panel a) and 289° - 300° (panel d) (Roth et al. 2021).  
187 Adding two other sets of observation allow us to highlight the orbital variability of Ganymede's  
188 atmosphere. The 135.6 nm / 130.4 nm emission intensity ratio at the center of the disk (all pixels inside  
189 < 0.5 R<sub>G</sub>) is lower than ~1.0 at a phase angle of 289° - 300° (panel d), i.e. when the trailing hemisphere  
190 is observed. It is slightly higher with values around 1-1.5 on the subjovian (335°- 340°, panel b) and  
191 antijovian sides (173°-177°, panel c) and peaking at a value around 2.0 at a phase angle of 98° - 111°  
192 (panel a, wake or leading hemisphere). If interpreted with the H<sub>2</sub>O abundance reducing the ratio, the  
193 observations of a systematically lower ratio at the four orbital positions implies that the H<sub>2</sub>O  
194 atmosphere is not transient but constantly present. The value of the oxygen emission ratio is around  
195 2.5 at the limb at all four orbital positions.

196 We note that the propagated uncertainty of the OI ratio near the disk center in the profiles of the  
197 newly added images is particularly high, allowing in principle for values consistent with (almost) only  
198 O<sub>2</sub> in the atmosphere. However, when integrating all pixels within 0.8 R<sub>G</sub> for the phase angle 335°-  
199 340° images (panel b, corresponding to the first 2 radial bins), we find a OI ratio of  $1.4 \pm 0.8$ , which is  
200 slightly outside the 1-sigma bounds for a pure O<sub>2</sub> atmosphere. Integrating over all pixels withing 0.6  
201 R<sub>G</sub> for the phase angle 173° - 177° image (panel c, ~2.4 bins), the OI ratio of  $1.1 \pm 0.5$  is inconsistent  
202 with pure O<sub>2</sub> at a 2-sigma level. Thus, also only marginally significant, the radial trend in the OI ratio  
203 found by Roth et al. (2021) is also present in the new two datasets.

204 The 2D images of the emission brightness might help us to explain this variability, with auroral regions  
205 closer to the center of the disk at  $98^\circ - 111^\circ$  and  $173^\circ - 177^\circ$  than at  $289^\circ - 300^\circ$  and  $335^\circ - 340^\circ$ . As  
206 shown in Marconi (2007), Ganymede's atmosphere is probably composed of  $\text{H}_2\text{O}$  and  $\text{O}_2$  and of their  
207 products, with a denser  $\text{O}_2$  atmosphere in the polar auroral regions and an  $\text{H}_2\text{O}$  atmosphere essentially  
208 produced by sublimation around the subsolar region. In another way, at phase angles of  $98^\circ - 111^\circ$ , the  
209 auroral regions are close to the center of the apparent disk, that is, to a region dominated by  $\text{H}_2\text{O}$   
210 leading to a low ratio of the two O emission lines. At  $177^\circ$ , the auroral regions are close to the limb far  
211 from the subsolar region, in a region of the exosphere dominated by  $\text{O}_2$  leading to a higher ratio of  
212 these two O emission lines.

213

214 In order to properly compare observation and simulation, there are three effects that should be  
215 considered because they can degrade the spatial resolution when observing Ganymede with HST/STIS:

- 216 • the pixel resolution of the instrument which is about 80 km,
- 217 • the PSF-smearing of about 2-2.5 pixels,
- 218 • the spectral smearing due to the dispersion included in the telescope setup. This will be small  
219 and not distinguishable from spatial effects. We neglect the effects in our modelling.

220 The first two effects are taken into account by projecting the simulated image on a grid with 80 km  
221 resolution and then convolving this with a 2D Lorentzian with a FWHM of 2.5 pixels.

222

### 223 **III Exospheric Global Model**

#### 224 **III.1 Description of the model**

225 The Exospheric Global Model (EGM) is a 3D time dependent Monte Carlo model that describes the fate  
226 of atmospheric species ejected from Ganymede's surface, moving under the influence of Ganymede  
227 and Jupiter gravity fields, being absorbed or reejected when reimpacting the surface and eventually

228 ionized or dissociated by photon and electron impacts. All products of water and O<sub>2</sub> are described, that  
 229 is, H<sub>2</sub>O, H, H<sub>2</sub>, O, O<sub>2</sub> and OH. EGM can also describe the effects of collision between these species in  
 230 the case of weakly dense atmosphere but in the following we will present simulations performed by  
 231 neglecting collisions between atmospheric species. Indeed, as explained in Leblanc et al. (2017),  
 232 collisions have a limited impact on the 3D large scale structure of the atmosphere and would not  
 233 change the conclusions of this present work. All details regarding EGM can be found in Leblanc et al.  
 234 (2017). EGM is time dependent so that it allows to follow the trajectory of the exospheric particles all  
 235 along Ganymede rotation around Jupiter. It therefore takes into account the centrifugal and Coriolis  
 236 forces applied on these particles due to Ganymede rotation in Jupiter frame and the variations of the  
 237 solar illumination (including the shadow induced by Jupiter) during Ganymede's orbit.

238 With EGM, we reconstruct in 3D the density, bulk velocity and temperature of all neutral species  
 239 around Ganymede. In order to reconstruct the emission intensity, we consider the various electron  
 240 and photon induced reactions that could produce the 130.4 nm, 135.6 nm or 121.6 nm emissions. In  
 241 the case of electron impact induced emission excitation, we considered various laboratory  
 242 measurements as listed in the fourth column of Table 1. The calculated emission rates at an energy of  
 243 100 eV are close to the ones used in Roth et al. (2021), as displayed in the second and third columns  
 244 of Table 1, except for electron impact on O impact leading to 135.6 nm emission for which we used  
 245 different cross sections than in Roth et al. (2021). For photon impact emission excitation, we used  
 246 previously published rates as indicated in Table 1.

Reactions	Rate for electrons at 100 eV (Roth et al. 2021)	Rate for electrons at 100 eV (This work)	Reference
O <sub>2</sub> + e → 1356 Å	3.7×10 <sup>-9</sup> cm <sup>3</sup> s <sup>-1</sup>	3.8×10 <sup>-9</sup> cm <sup>3</sup> s <sup>-1</sup>	Kanik et al. (2003)
O <sub>2</sub> + e → 1304 Å	1.57×10 <sup>-9</sup> cm <sup>3</sup> s <sup>-1</sup>	1.72×10 <sup>-9</sup> cm <sup>3</sup> s <sup>-1</sup>	
O + e → 1356 Å	0.195×10 <sup>-9</sup> cm <sup>3</sup> s <sup>-1</sup>	0.24×10 <sup>-10</sup> cm <sup>3</sup> s <sup>-1</sup>	Tayal et al. (2016)

$O + e \rightarrow 1304 \text{ \AA}$	$4.84 \times 10^{-9} \text{ cm}^3 \text{ s}^{-1}$	$5.38 \times 10^{-9} \text{ cm}^3 \text{ s}^{-1}$	Johnson et al. (2005)
$H_2O + e \rightarrow 1304 \text{ \AA}$	$0.16 \times 10^{-9} \text{ cm}^3 \text{ s}^{-1}$	$0.19 \times 10^{-9} \text{ cm}^3 \text{ s}^{-1}$	Makarov et al. (2004)
$H_2O + e \rightarrow 1356 \text{ \AA}$	$0.32 \times 10^{-10} \text{ cm}^3 \text{ s}^{-1}$	$0.37 \times 10^{-10} \text{ cm}^3 \text{ s}^{-1}$	Rate at 130.4 nm divided by 5 (Roth et al. 2021)
$H_2 + e \rightarrow 1216 \text{ \AA}$	Not available	$3.2 \times 10^{-9} \text{ cm}^3 \text{ s}^{-1}$	Ajello et al. (1995)
$H_2O + e \rightarrow 1216 \text{ \AA}$	Not available	$4.2 \times 10^{-9} \text{ cm}^3 \text{ s}^{-1}$	Makarov et al. (2004)
<b>Reactions</b>	<b>Excitation rate</b>		<b>Reference</b>
$H_2O + h\nu \rightarrow H + H +$ $O \ 1216 \text{ \AA}$	$1.4 \times 10^{-10} \text{ s}^{-1}$		Roth et al. (2014)
$H + h\nu \rightarrow 1216 \text{ \AA}$	$7.29 - 11.8 \times 10^{-5} \text{ s}^{-1}$		Alday et al. (2017)
$O + h\nu \rightarrow 1304 \text{ \AA}$	$4.0 \times 10^{-7} \text{ s}^{-1}$		Roth et al. (2021)

247 **Table 1:** Reactions and rates used to calculate the emission intensity at 1304, 1356 and 1216 Å.

248 In Leblanc et al. (2017), we discussed two scenarios for the production of H<sub>2</sub>O. One case with low  
249 sublimation rate (hereafter the dry exospheric case) is inconsistent with the H<sub>2</sub>O/O<sub>2</sub> ratios from Roth  
250 et al. (2021) for O<sub>2</sub> column densities higher than  $1 \times 10^{13} \text{ cm}^{-2}$ , as generally assumed to be the case for  
251 Ganymede (Hall et al. 1998, Johnson et al. 2004). The second case used nominal sublimation rate as  
252 calculated from Fray and Schmitt (2009) parametrization of the sublimation of water ice at very low  
253 pressure and cold temperature. Using the nominal sublimation rate scenario, we here simulate five  
254 consecutive orbits of Ganymede around Jupiter following around  $2 \times 10^6$  test-particles at each time step  
255 of 0.25 s. Few hundred thousand test-particles were used to describe each of the 6 species, namely,  
256 H, H<sub>2</sub>, O, OH, H<sub>2</sub>O and O<sub>2</sub> with weight values between  $10^7$  to  $10^{16}$  (number of real particles represented  
257 by each test-particle). The macroscopic quantities like density, velocity, temperature, escape flux and  
258 reabsorbed surface flux are reconstructed on a 100 (along the radial direction)  $\times$  50 (along the polar  
259 direction)  $\times$  100 (along the azimuth direction) spherical grid. A typical run lasts one to two weeks on

260 64 CPUs. Four orbits are needed in order to reach a steady solution with no significant difference in  
261 the 3D reconstructed macroscopic parameters between the two last orbits.

262 The characteristics of the electron population at the origin of the auroral emissions remain poorly  
263 constrained by observation. Roth et al. (2021) assumed an effective averaged homogeneous electron  
264 density with values between 20 and 30  $\text{cm}^{-3}$ , an electronic temperature of 100 eV and global  $\text{O}_2$   
265 abundances of  $\sim 3 \times 10^{14} \text{ O}_2/\text{cm}^2$ , which yields effective 135.6 emission brightnesses primarily produced  
266 by impact of electrons on  $\text{O}_2$  (see Figure 3) in the range of the observed values. As discussed in Carnielli  
267 et al. (2020a), the original  $10^{14} - 10^{15} \text{ O}_2/\text{cm}^2$  suggested by Hall et al. (1998) is based on the upper limit  
268 set by a stellar occultation observation performed by Voyager 1 (Broadfoot et al. 1979) which  
269 suggested actually an upper limit at  $2.5 \times 10^{15} \text{ cm}^{-2}$  (Carnielli et al. 2020a). Carnielli et al. (2020a)  
270 reconstructed the ionospheric density, compared the resulting density to the G2 flyby measurements  
271 for the case of a dry exosphere (Leblanc et al. 2017) and concluded that both exospheric content and  
272 electron ionization rate might have been underestimated in previous modelling (Marconi 2007;  
273 Leblanc et al. 2017) illustrating the difficulty to derive from the auroral emission observations an  
274 accurate estimate of Ganymede's atmospheric content without knowing the electron density and  
275 temperature. Eviatar et al. (2001) using a simple auroral model (or more specifically, the electron  
276 energy spectral flux measured by Galileo over the auroral region) suggested that the electron density  
277 responsible for Ganymede's auroral emissions should be closer to a few hundred  $\text{cm}^{-3}$  rather than few  
278 ten of  $\text{cm}^{-3}$ . Such a much larger electron density would mechanically imply a much less dense  
279 exosphere in the auroral regions to explain the observed auroral brightnesses except if the electron  
280 temperature is significantly smaller than supposed by these authors.

281 In the following, we chose to use an electron population at 100 eV. A uniform reaction rate  
282 corresponding to the rate displayed in Table 1 multiplied by an electron density of  $20 \text{ cm}^{-3}$  is assumed  
283 everywhere except over the auroral ovals. A locally increased reaction rate is set over the latitudes  
284  $\pm 10^\circ$  of the OCFB (see Figure 3 of McGrath et al. 2013 and Figure 3 of Leblanc et al. 2017) and  
285 corresponds to the rate displayed in Table 1 multiplied by an electron density of  $70 \text{ cm}^{-3}$ . The  $\pm 10^\circ$  was



286 chosen to reproduce roughly the observed latitudinal width (c.f. Musacchio et al. 2017, their figure 9)  
 287 and corresponds to the current structure in Ganymede’s magnetosphere as modelled by Jia et al.  
 288 (2009). The ejection mechanisms at the origin of Ganymede’s exosphere are also constrained using  
 289 this same separation between open and close field line regions as described in Leblanc et al. (2017).

290

291 III.2 Ganymede’s exosphere as modelled by EGM

292 Table 2 provides the surface ejection rate for the 7 species described in EGM for the nominal  
 293 sublimation rate and sputtering conditions. With the exception of water molecules which can be  
 294 ejected by sublimation, most of the species are ejected from the surface by sputtering or radiolysis  
 295 induced ejection. The typical rates are close to the ones used in Marconi (2007). When comparing the  
 296 source rates with the neutral escape rates, we can see that loss and source terms are never equal  
 297 which implies that surface reabsorption, photon and electron impact dissociation and photon and  
 298 electron impact ionization are important loss mechanisms. Vorburger et al. (2021) recently published  
 299 a detailed modelling of Ganymede’s exosphere. They concluded that Leblanc et al. (2017) sputtering  
 300 water rate was up to two orders larger than the ones of other models. It is unclear what the origin of  
 301 these discrepancies is, our reconstructed yield being based on Cassidy et al. (2013) analysis derived  
 302 from a large set of laboratory measurements.

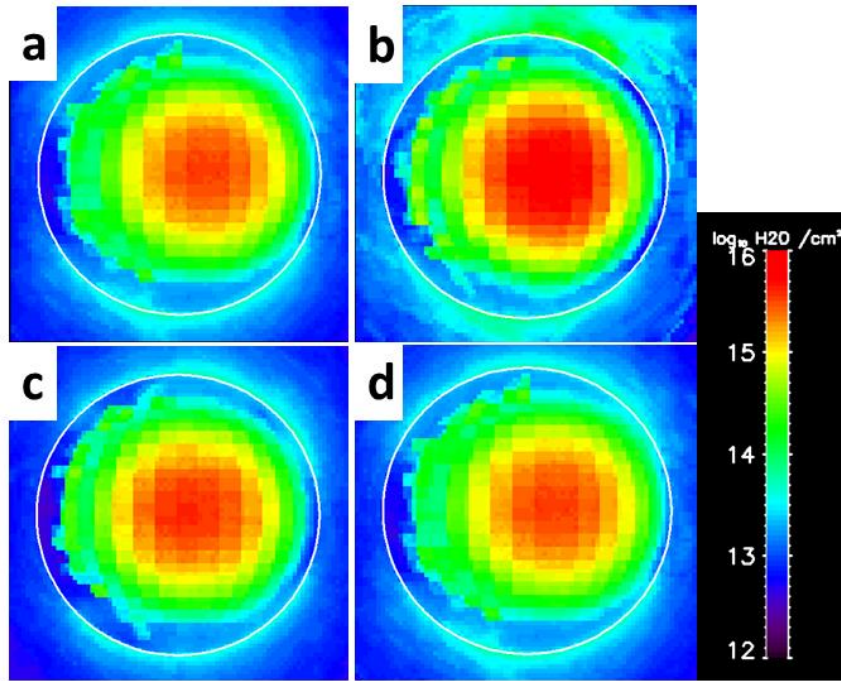
Species		H	H <sub>2</sub>	O	OH	H <sub>2</sub> O		O <sub>2</sub>
Source		Sputtering	Sputtering	Sputtering	Sputtering	Sputtering	Sublimation	Sputtering
Rate (s <sup>-1</sup> )	Surface ejection	2.0×10 <sup>25</sup>	8.3×10 <sup>26</sup>	1.0×10 <sup>25</sup>	1.0×10 <sup>25</sup>	4.0×10 <sup>27</sup>	8.0×10 <sup>29</sup>	4.4×10 <sup>26</sup>
	Escape	2.9×10 <sup>26</sup>	2.7×10 <sup>26</sup>	1.0×10 <sup>26</sup>	4.0×10 <sup>25</sup>	7.0×10 <sup>26</sup>		4.4×10 <sup>15</sup>

303 **Table 2:** Simulated source and neutral escape rates (average values on 2 consecutive orbits)

304 In the case of the atomic H exosphere, the neutral escape rate is 10 times larger than the sputtering  
 305 rate which is due to the fact that most of the H atoms are produced from the dissociation of H<sub>2</sub>O and  
 306 H<sub>2</sub>. Moreover, dissociation produces H atoms with enough energy to be lost by neutral escape. A small

307 fraction of these H atoms is also reabsorbed by the surface or ionized. In the simulation, H<sub>2</sub> is not  
308 reabsorbed by the surface by assumption (see Leblanc et al. 2017), so that H<sub>2</sub> molecules either escape  
309 as neutral particle, are dissociated or are ionized. Oxygen atoms can be sputtered from the surface but  
310 are also the products of the dissociation of O<sub>2</sub> and H<sub>2</sub>O. A large proportion of the O atoms are  
311 reabsorbed in the surface. In the same way, OH is either ejected from the surface by sputtering or  
312 produced from the dissociation of H<sub>2</sub>O exospheric molecules. The main source of the H<sub>2</sub>O exosphere  
313 is sublimation, the sputtering rate being of less than one percent of the sublimation one. Most of the  
314 H<sub>2</sub>O molecules ejected from the surface are reabsorbed in the surface. Contrary to the other  
315 exospheric species, O<sub>2</sub> is too heavy to escape Ganymede gravity as neutral so that its ejection rate is  
316 balanced by the dissociation and ionization rates. Numerically, a simulation of more than 4 orbits is  
317 needed to reach a steady state between loss and source for this species.

318 In Figures 4 and 5, we display how Ganymede's H<sub>2</sub>O and O<sub>2</sub> exospheric column densities would be seen  
319 from the Earth at the four positions of HST/STIS observations described in Figure 1. As expected and  
320 described in many past publications (see example, Marconi 2007; Plainaki et al. 2015; Leblanc et al.  
321 2017; Plainaki et al. 2020), the H<sub>2</sub>O exosphere is spatially organized compared to the O<sub>2</sub> exosphere,  
322 with a peak near the subsolar point for the H<sub>2</sub>O whereas the O<sub>2</sub> column density peaks around the limb  
323 with slightly larger values near the poles. As explained in Leblanc et al. (2017), Oza et al. (2019) and  
324 Johnson et al. (2019), Ganymede's orbital motion leads to a slightly shift of the H<sub>2</sub>O peak towards the  
325 dusk side.



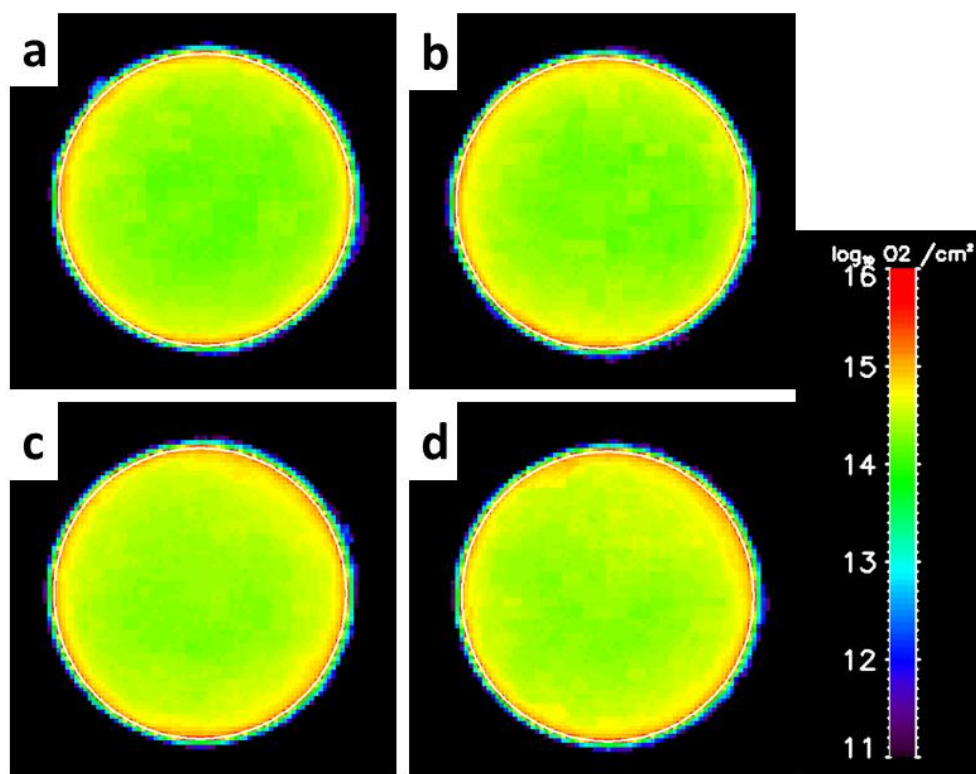
326

327 **Figure 4:** Simulated column densities of the H<sub>2</sub>O exospheric component (in log<sub>10</sub> cm<sup>-3</sup>) at the four  
 328 positions of Figure 1 in the nominal simulation case. Panel a: phase angle of 98°-111°. Panel b: phase  
 329 angle of 335°-340. Panel c: phase angle of 173° - 177°. Panel d: phase angle between 289° - 300°. The  
 330 subsolar point is at the center of each panel. Dawn is on the left of each panel, the North being towards  
 331 the top. Ganymede limb is represented by the white circle.

332

333 Whereas we observe a significant change with respect to Ganymede orbital positions in the H<sub>2</sub>O  
 334 exosphere as seen from the Earth, the O<sub>2</sub> exosphere does not appear to vary in terms of global  
 335 distribution. The water orbital variability is related to the change in surface albedo between leading  
 336 and trailing sides of Ganymede (Spencer 1987) leading to a variation between 146 (maximum on the  
 337 trailing side) to 142 K (minimum on the leading side) of the subsolar surface temperature and to an  
 338 order of magnitude variation of the sublimation rate (see Figure 2 in Leblanc et al. 2017). The maximum  
 339 H<sub>2</sub>O column density around the subsolar region reaches values of few 10<sup>15</sup> H<sub>2</sub>O/cm<sup>2</sup> near the surface  
 340 (and a peak density around 10<sup>9</sup> H<sub>2</sub>O/cm<sup>3</sup> at the surface with atmospheric temperature close to the  
 341 surface one up to 400 km in altitude) and decreases to a plateau at 10<sup>13</sup> H<sub>2</sub>O/cm<sup>2</sup> from 500 km to few

342 thousands km in altitude (corresponding to temperature around 2000 K above 800 km). These two-  
 343 slope profile is related to the two main sources of H<sub>2</sub>O sputtering and sublimation (Table 2). The only  
 344 change that can be inferred from the 2D images of the O<sub>2</sub> column density is due to the latitudinal  
 345 extension of the polar regions which is closer to the equator when the leading side of Ganymede is  
 346 illuminated (Figures 2 panels a and c) with respect to the trailing side illuminated hemisphere. The O<sub>2</sub>  
 347 column density peaks at a value of 10<sup>15</sup> O<sub>2</sub>/cm<sup>2</sup> at the surface (and a density of 10<sup>8</sup> O<sub>2</sub>/cm<sup>3</sup>) and  
 348 decreases by three to four orders of magnitude within the first 100 km in altitude.



349

350

**Figure 5:** Same as in Figure 4 but for the O<sub>2</sub> column density.

	Phase angle 98°- <b>111°</b>	Phase angle 173° <b>- 177°</b>	Phase angle 289° <b>- 300°</b>	Phase angle <b>335°-340°</b>
H	2.5×10 <sup>+11</sup>	1.2×10 <sup>+11</sup>	2.8×10 <sup>+11</sup>	2.2×10 <sup>+11</sup>
H <sub>2</sub>	5.6×10 <sup>+14</sup>	6.1×10 <sup>+14</sup>	5.0×10 <sup>+14</sup>	4.6×10 <sup>+14</sup>
H <sub>2</sub> O	5.6×10 <sup>+14</sup>	6.4×10 <sup>+14</sup>	1.3×10 <sup>+15</sup>	1.0×10 <sup>+15</sup>

O	$1.6 \times 10^{12}$	$2.5 \times 10^{12}$	$1.0 \times 10^{12}$	$1.1 \times 10^{12}$
O <sub>2</sub>	$4.3 \times 10^{14}$	$4.3 \times 10^{14}$	$3.6 \times 10^{14}$	$3.7 \times 10^{14}$
OH	$1.5 \times 10^{12}$	$1.5 \times 10^{12}$	$1.2 \times 10^{12}$	$4.7 \times 10^{12}$

351 **Table 3:** Simulated disk averaged column densities in  $\text{cm}^{-2}$  for the nominal sublimation and sputtering  
 352 *rate conditions*

353 As illustrated in Figures 4, 5 and Table 3, there is some orbital dependency of Ganymede's exosphere  
 354 which are essentially driven by the leading/trailing variation of the albedo which controls the  
 355 sublimation rate of the H<sub>2</sub>O and in a lesser way the efficiency of the sputtering (Cassidy et al. 2013).  
 356 Whereas the O<sub>2</sub> and H<sub>2</sub> average column densities do not change significantly along Ganymede's orbit,  
 357 the H<sub>2</sub>O exosphere column density displays a clear variation. According to Table 3, Ganymede's  
 358 exosphere is always dominated by water molecules in an average over the full disk.

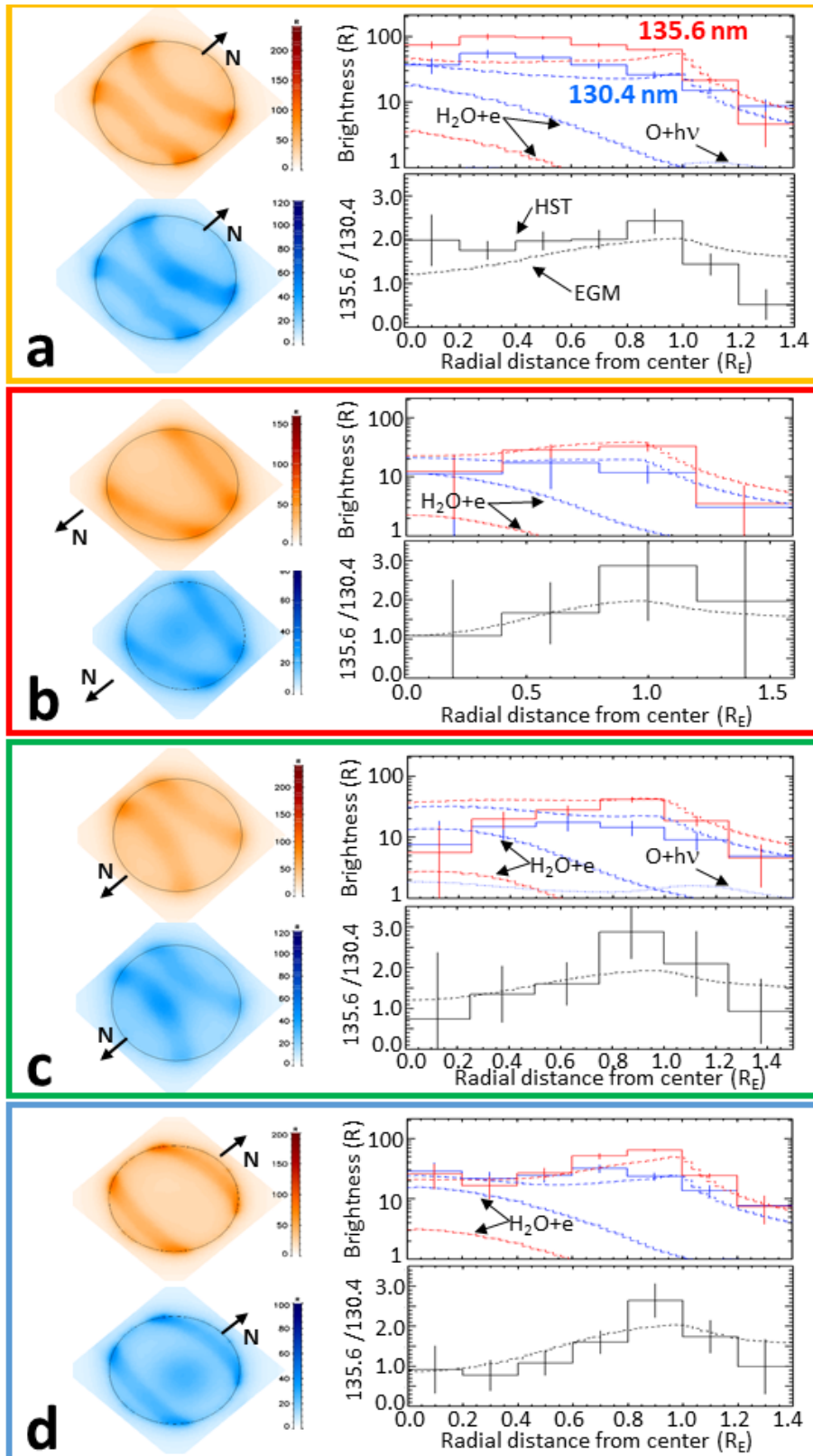
359

#### 360 **IV Comparison with HST observations**

##### 361 *IV.1 Reconstructed oxygen emissions*

362 All together, the agreement between observation and simulation using the nominal sublimation rate  
 363 (section III.2) as displayed in Figure 6 is remarkably good considering that we did not make any change  
 364 of the exospheric model and used a fixed temperature and density of the electrons responsible for the  
 365 auroral emission (section III.1). There are however still several discrepancies between the simulated  
 366 profiles (right panels in each rectangle) which could be either due to the electron population  
 367 description or due to the exospheric description as discussed in the following.

368



369

370 **Figure 6:** Comparison between observation of Ganymede's atmospheric emission by HST/STIS and EGM  
 371 simulation. Each panel corresponds to one date. a 2010-11-19, phase angle of  $98^{\circ}$ - $111^{\circ}$  (Roth et al.  
 372 2021). b: 2003-11-30, phase angle of  $335^{\circ}$ - $340^{\circ}$  (McGrath et al. 2013). c: 2017-02-02, phase angle of

373 173°-177°. d: 1998-10-30, phase angle between 289° - 300° (Roth et al. 2021). Each panel surrounded  
374 by a rectangle which colour corresponding to Figure 1 circle colours is composed of the simulated  
375 images of the 1356 Å (red) and 1304 Å (blue) brightness intensities, of the radial profile from the center  
376 of the disk up to around half a radius above the limb of the emission brightness intensity for these  
377 wavelength (top right panel in each rectangle with in solid line, HST/STIS observations, in dashed lines,  
378 EGM reconstructed emission intensity, in dashed-dotted lines, EGM emission intensity from  $H_2O+e$   
379 reaction and in dotted line, EGM emission intensity from  $O+h\nu$  reaction) and of the ratio of these two  
380 emission lines 1356 emission intensity divided by 1304 emission intensity (bottom right panel in each  
381 rectangle).

382

383 Starting from panel a, at a phase angle of 98°-111°, that is looking to Ganymede when its leading side  
384 faces the Sun, the measured 135.6 nm emission (red solid line) is underestimated by 50% by the  
385 simulation on the disk (below a radial distance of  $0.8 R_G$ ). The observed 130.4 nm emission (solid blue  
386 line) is also slightly underestimated. The 135.6 nm emission being produced by electron impact on the  
387  $O_2$  molecule (the dashed-dotted red line corresponds to the emission intensity produced by electron  
388 impact on  $H_2O$  molecules which is then one order smaller), a 50% denser  $O_2$  exosphere on the  
389 illuminated leading side or an electron density larger by 50% (that is an electron density  $\sim 100 \text{ cm}^{-3}$  in  
390 the auroral regions) would lead to a much better reproduction of the observations close to the center  
391 of the disk. At the limb (above  $1 R_G$ ), the ratio of the two observed emission lines decreases down to a  
392 value around 0.5, showing either an increase of the amount of  $H_2O$  molecules at the origin of these  
393 emissions or an increase of the atomic oxygen abundance. Roth et al. (2021) suggested that the oxygen  
394 atoms should get more abundant in the exosphere at higher altitude being among the less massive  
395 species. Clearly, if it is the case, the model underestimates this population. Oxygen atoms can come  
396 either from the dissociation of the  $O_2$  and  $H_2O$  or directly from the surface sputtering. Since increasing  
397 the  $O_2$  and  $H_2O$  densities, in particular close to the limb, would lead to a discrepancy with the

398 observations, the most plausible explanation is that the flux of O atoms sputtered from the surface is  
399 underestimated by the model. We therefore tested much larger ejection rate by sputtering of the O  
400 atoms, by up to a factor 100, and simulated an exosphere with emissions closer to the ones reported  
401 in Figure 2 but still not matching the observed emission brightness ratio at  $1.3 R_G$  from the limb. The  
402 reconstructed 2D images of the emission brightness as displayed in Figure 6a (left) reproduced the  
403 shape of the auroral emissions, logically since we imposed it arbitrarily in our reconstruction of these  
404 emissions, through the increase in electron density around the OCBF (see section III). We also  
405 simulated a limb asymmetry between dawn and dusk, an asymmetry due to the asymmetry of the  
406 exosphere as seen from the Earth. Such asymmetry in the auroral emissions might be also related to  
407 the electron current system as discussed by Musacchio et al. (2017).

408 At a phase angle around  $335^\circ - 340^\circ$  (panel b in Figure 6), the Sub-Jovian hemisphere of Ganymede  
409 faces the observer. For such case, the model results are in rather good agreement with the  
410 observation, the emission brightness intensities of the two emission lines and their ratio being  
411 reproduced by the model within the uncertainties of the observation. A similar excellent agreement  
412 between simulation and observation is also obtained at a phase angle of  $289^\circ - 300^\circ$  (panel d). However,  
413 at  $0.9 R_G$  from the center of the disk, the observed ratio reaches a value above 2.5. Even with a pure  
414  $O_2$  exosphere, maximum values around 2 would be produced according to Figure 3d, making a ratio of  
415 2.5 very unlikely with only a mixture of  $H_2O$  and  $O_2$ .

416 The comparison between simulated emission brightness intensity and observed ones in panel c (phase  
417 angle of  $173^\circ - 177^\circ$ ) displays significant discrepancies. Close to the center of the disk, the model  
418 calculated an emission brightness much more intense than observed, by a factor 6 for the 135.6 nm  
419 emission and a factor 4 for the 130.4 nm emission. At this orbital position, Ganymede's anti-Jovian  
420 hemisphere faces the observer. A potential reason for the observed decrease in the emission  
421 brightness intensity close to the center of the disk at such orbital position might be therefore related  
422 to the dependency of the current system at the origin of these auroral emissions with respect to the



423 ram/wake orientation and Jovian/Anti-Jovian hemisphere, a dependency that we did not consider  
424 when adopting constant density and energy of the electron in the auroral bands. A smaller density of  
425 the electron at the origin of these emissions would lead to a less intense emission intensity but to a  
426 similar value of their ratio. At the limb, the observed emission lines have similar intensities, leading to  
427 a ratio close to one. The simulation predicts a ratio close to 1.5 which is consistent with the observation  
428 when considering the uncertainty on the observed ratio. At  $0.8 R_G$  from the center of the apparent  
429 disk, this same ratio reaches a value of  $2.8 \pm 0.7$ . If real, it would suggest a mechanism for the production  
430 of these emissions which is not taken into account in our model.

431 To summarize, the nominal sublimation model of Ganymede's exosphere convolved with the simple  
432 description of the population of electron at the origin of the observed emission leads to a good  
433 agreement with the observation on the side of the orbit when Ganymede trailing hemisphere is facing  
434 the Sun. We obtained a less good agreement on the other side. In the exospheric model, the only  
435 difference taken into account between these two portions of the orbit is related to the change of the  
436 wake/ram angle with respect to the subsolar/anti-solar direction. The most probable origin of this  
437 discrepancy is related to the simple description of the electron population leading to these auroral  
438 emissions. This population has been shown to be variable and dependent on the wake/ram, Sub-solar  
439 – anti-jovian axis and to the sub-solar direction (Jia et al. 2009; Sauer et al. 2015). As a matter of fact,  
440 Carnielli et al. (2020a) reconstructed the ionosphere of Ganymede using Leblanc et al. (2017) dry  
441 exospheric model and concluded that the density of ionising electrons is denser than previously  
442 inferred from Galileo (Carnielli et al. 2019) at (or extrapolated to) Ganymede's orbit so that the  
443 electron impact ionization frequency should be increased by a factor 4 in the anti-Jovian hemisphere  
444 for the G2 flyby conditions. As a matter of fact, recent radio-occultation observations performed during  
445 JUNO flyby of Ganymede suggest an electron density close to the surface of  $2000 \pm 500 \text{ cm}^{-3}$  in the open  
446 magnetic field regions of Ganymede magnetosphere (Buccino et al. 2022). A higher ionisation  
447 frequency is also consistent with our conclusions that to reproduce the observed emission profiles  
448 above the limb, a higher electron impact dissociation rate of  $\text{O}_2$  is needed. Carnielli et al. (2020a) also

449 concluded that the O<sub>2</sub> density in the polar regions should be increased by a factor 10 with respect to  
450 the dry scenario (Table 3). The nominal sublimation scenario used here leads to H<sub>2</sub>O average column  
451 densities 30 to 100 times denser than in the dry scenario (Leblanc et al. 2017). However, a nominal  
452 sublimation rate scenario might be not enough to reproduce Galileo electron density at high latitudes,  
453 since the H<sub>2</sub>O exosphere is essentially concentrated in the sublimation equatorward region. Moreover,  
454 a 10 times denser O<sub>2</sub> exosphere convolved with a higher electron impact rate, would probably lead to  
455 a significantly larger 135.6 nm / 130.4 nm ratio in the auroral regions in disagreement with the  
456 observations (Figure 6). Without a detailed knowledge of the electron density and temperature in the  
457 open field lines regions, it is therefore not realistic to conclude firmly on how to reconcile measured  
458 electron density and auroral emission intensities. We note, however, that the 135.6 nm / 130.4 nm  
459 ratio for O<sub>2</sub> is similar within the relevant electron temperatures range (e.g. Kanik et al. 2003 and Figure  
460 3d). If the ratio for H<sub>2</sub>O is similarly insensitive to the temperature as supposed in Figure 3d, firm  
461 conclusions are possible without exact knowledge of the absolute excitation and brightnesses.

462 As discussed before, the ratio of the two measured emission lines above the limb suggests an  
463 underestimate of the O population by EGM in this region. We simulated much larger sputtering rate  
464 of the O atoms (by a factor 100) from the surface without changing significantly the simulated ratio  
465 displayed in Figure 6. The main reason is that the main source of the O exospheric population is not its  
466 sputtering from the surface but the dissociation of O<sub>2</sub> and H<sub>2</sub>O. We therefore performed a simulation  
467 with an electron impact rate increased by a factor 2.0 in the open field lines region (equivalent to  
468 increase the electron density by a similar factor). However, increasing the electron impact dissociation  
469 also leads to a lower density of both molecules and therefore a smaller brightness intensity at 130.4  
470 and 136.6 nm. We had therefore to increase by a factor 1.8 the sputtering rate of both O<sub>2</sub> and H<sub>2</sub>O to  
471 compensate the increase in their dissociation rate to fit the observed emission brightness. We also had  
472 to increase the sputtering rate for O and H with respect to the one of O<sub>2</sub> by a factor 40 in order to  
473 retrieve emission brightness ratio above the limb close to the ones observed by HST. With such  
474 increase of the sputtering rate of H and O, sputtering is equivalent to the dissociation of O<sub>2</sub> and H<sub>2</sub> as

475 source for these two exospheric species. The density for these two species significantly increased by  
476 more than an order of magnitude in the case of H and by a factor 2 to 3 in the case of the O exosphere.  
477 In that case, the simulated O column density is marginally larger than the upper limit set by Roth et al.  
478 (2021) for the column density by a factor 2.5. The other species, namely H<sub>2</sub>, O<sub>2</sub>, H<sub>2</sub>O and OH, remains  
479 almost unchanged with respect to the nominal species.

480

#### 481 *IV.2 Reconstructed H emission*

482 Lyman  $\alpha$  emission from Ganymede's atmosphere was detected for the first time by Galileo (Barth et  
483 al. 1997) and later confirmed from HST by Feldman et al. (2000). Recently, Alday et al. (2017) provided  
484 a detailed analysis of four sets of HST observations obtained between 1998 and 2014. These authors  
485 estimated the emission brightness from Ganymede's corona (outside from the apparent disk) as  
486 ranging from 0 to 450 R for a phase angle between 77.9° and 103.5° (average emission of 215±66 R),  
487 from 110 to 310 R for a phase angle between 269.3° and 291.8° (average emission of 180±52 R). As  
488 discussed in Alday et al. (2017), the globally lower emission intensities of the Lyman  $\alpha$  emission  
489 obtained in 2014 with respect to the other set of observations obtained in 1998, 2010 and 2011 are  
490 probably due to strong absorption of the emission by the geocorona. Excluding these 2014  
491 observations, the Lyman  $\alpha$  emission brightness between 90.1° and 103.5° is 328±159 R and at 291.8°  
492 is 310 R.

493 In order to predict brightnesses, we simulated the emission brightness at Lyman  $\alpha$  using the various  
494 possible excitation processes described in Table 1 for the nominal exosphere case. At a phase angle of  
495 98° - 111°, the emission brightness intensity at Lyman  $\alpha$  was simulated as being equal to 170 Rayleigh  
496 on the apparent disk and 47 Rayleigh outside. On the disk, H<sub>2</sub>O electron impact emission dominates  
497 with 100 Rayleigh induced by this process and 50 Rayleigh is associated with H<sub>2</sub> electron impact.  
498 Outside of the disk, H<sub>2</sub>O electron impact induces only 9 Rayleigh of emission intensity and 25 Rayleigh  
499 is produced by H<sub>2</sub> electron impact. Very similar values are simulated at a phase angle of 289° - 300°.

500 These H Lyman-alpha aurora intensities are not discernible from the other sources in the HST  
501 observations and therefore not detectable. For resonant scattering by H atoms, we get intensities on  
502 the order of 10-20 Rayleigh for our simulations. With respect to the reported emission intensity in the  
503 extended corona outside of the disk with peak brightness near the moon of ~300 R (Alday et al. 2017),  
504 our simulated intensities are therefore an order of magnitude too low.

505 The only way to increase the simulated emission intensity would be to increase the density in H atoms.  
506 exospheric H atoms are produced either from direct sputtering from the surface or coming from the  
507 dissociation of H<sub>2</sub>O and H<sub>2</sub>. Increasing the H<sub>2</sub>O or H<sub>2</sub> dissociation rate is possible by increasing the H<sub>2</sub>O  
508 or H<sub>2</sub> density but this would lead to a disagreement between simulation and observation regarding the  
509 OI 130.4 nm and 135.6 nm emission line profiles (Figure 6). It is also possible that the dissociation  
510 frequency used in our simulation for these two molecules is underestimated because of a higher  
511 electron density or temperature. Increasing the electron energy would lead to a small increase of the  
512 electron impact dissociation, the typical electron impact dissociation cross section with respect to the  
513 electron energy forming a plateau above 20 eV for H<sub>2</sub>+e → H + H (Dalgarno et al. 1999) or peaking  
514 around 100 eV for H<sub>2</sub>O+e → H+OH and H<sub>2</sub>O + e → H+H+O (Song et al. 2021). We performed a  
515 simulation where the electron impact rate is increased by a factor 2 through an increase of the electron  
516 density in the open field lines region, combined with a sputtering rate of the H atoms increased by a  
517 factor 72. In that case, between 98° and 111°, the H density in the corona of Ganymede is increased  
518 by a factor 10, leading to a stronger emission intensity from the corona equal to 450 Rayleigh on the  
519 disk and of 230 Rayleigh outside the disk (with 20 Rayleigh produced by electron impact on H<sub>2</sub> and 200  
520 by resonant scattering on H atoms). At a phase angle of 289° - 300°, the H corona is also increased by  
521 a factor 10 leading to an emission brightness of 300 Rayleigh on the disk and of 180 Rayleigh outside  
522 the disk (with 20 Rayleigh produced by electron impact on H<sub>2</sub> and 160 by resonant scattering on H  
523 atoms). Therefore, as concluded in the case of the oxygen atoms, a sputtering rate of H atoms from  
524 Ganymede surface increased by almost two orders of magnitude and a factor two increase of the

525 electron impact dissociation of  $H_2$  and  $H_2O$  with respect to the nominal value are needed to reproduce  
526 the brightness intensity of the Lyman  $\alpha$  extended exosphere of Ganymede.

527

## 528 **VI Conclusion**

529 Ganymede's atmosphere is thought to be composed of water molecules and its products (in particular  
530  $O_2$ ), thanks to several set of observations from Galileo and Hubble Space Telescope (HST) and to  
531 modelling (see Roth et al. 2021 for more details). Ganymede's atmosphere is probably unique in our  
532 solar system, in the sense, that it is not exactly a surface bounded exosphere as defined by Stern (1999)  
533 but is probably collisional locally. Indeed, it is partly produced by (1) the sublimation of its icy surface  
534 around the subsolar point which leads to a water molecular atmosphere locally thick enough to be  
535 collisional; and (2) for the rest of its surface, by the permanent bombardment of its surface by the  
536 Jovian and ionospheric electrons and ions leading to radiolysis and sputtering (Roth et al. 2021). The  
537 observation of Ganymede's atmosphere presented in Roth et al. (2021) provided for the first time the  
538 clear evidence of the presence of a thick water molecular atmospheric component as predicted by  
539 Marconi (2007). Roth et al. (2021) analysed a set of HST observations with a simple parametric  
540 description of Ganymede's atmosphere and derived the amount of water molecule that should be  
541 present around Ganymede. A recent study by de Kleer et al. (2023) measured optical oxygen emissions  
542 deriving a global upper limit on the  $H_2O/O_2$  ratio below Roth et al. (2021) derived ratios from aperture-  
543 integrated emissions brightnesses. Although the authors claim a conflict with Roth et al. (2021) results,  
544 they are in fact consistent: the majority of the emissions on the sub-Jovian are located near or above  
545 the limb. The globally integrated emission ratio, which de Kleer et al. use, is therefore only  
546 representative for this region and the lower line ratio on the disk center and the  $H_2O$  abundance there  
547 will remain undetected in their data.

548 In this paper, the newly published observations are taken such that the anti-Jovian and sub-Jovian  
549 hemispheres are observed, i.e. at intermediate geometries between the previously published leading

550 and trailing side observations (Roth et al. 2021). The new data show that the 135.6 nm/130.4 nm ratio  
551 in the Ganymede disk center is also intermediate, i.e., lower on the leading side but higher on the  
552 trailing side. This means that the oxygen emission ratio and related molecular abundances appear to  
553 be modulated by Ganymede's orbital period. Using a simplified description for the electron to  
554 reconstruct the electron impact excitation at the origin of HST observations, we showed that  
555 Exospheric Global Model (EGM; Leblanc et al. 2017) provides a rather good agreement with this set of  
556 observations obtained at four positions of Ganymede around its orbit. By modelling the orbital  
557 variability of the surface radiolysis and sublimation and their dependency with respect to the intrinsic  
558 Ganymede's magnetosphere and to the surface temperature, EGM succeeded to provide a consistent  
559 description of the origins of Ganymede's exosphere and of its content.

560 We found slightly smaller amount of water than Roth et al. (2021), with an average disk column density  
561 between  $0.5 \times 10^{+15}$  H<sub>2</sub>O/cm<sup>2</sup> when the leading hemisphere of Ganymede is illuminated and  $1.3 \times 10^{+15}$   
562 when it is the trailing hemisphere. The H<sub>2</sub>O atmosphere density on the sub-Jovian and anti-Jovian sides  
563 is in between these values, consistent with the observations. The O<sub>2</sub> atmosphere is less variable with  
564 an average disk column density around  $4.0 \times 10^{+14}$  O<sub>2</sub>/cm<sup>2</sup>, a relatively low abundance with respect to  
565 previous analysis (Hall et al. 1998). Our analysis also suggests that the spatial distribution of the  
566 exosphere should be slightly shifted towards the dusk side on the dayside, in particular for its H<sub>2</sub>O  
567 component. We also discussed the reconstructed Lyman  $\alpha$  emission brightness and compared it to  
568 observations (Alday et al. 2017) and showed that the model significantly underestimates the  
569 brightness intensity of this emission line far from Ganymede's surface. As for the oxygen emission lines,  
570 we concluded that to reproduce the emission brightness far from the surface, a much higher sputtering  
571 rate of the oxygen and hydrogen atoms is needed with respect to the nominal rate used in Leblanc et  
572 al. (2017) and previous publications. This higher sputtering rate should be also combined with a two  
573 times higher dissociation rate of the exospheric molecules close to Ganymede, suggesting a denser  
574 electron population with enough energy to dissociate the exospheric molecules in the open field line  
575 regions than supposed in Leblanc et al. (2017).

576 This paper provides the first consistent attempt to reconstruct of the observations that presently  
577 constrain Ganymede's exosphere. It also highlights the need to properly take into account the various  
578 possible sources of the auroral emissions, in particular the electron population. Without either in-situ  
579 measurements to better constrain this electron population, or detailed modelling of the ionosphere  
580 and its suprathermal electron component, any analysis of the auroral emissions observed around  
581 Ganymede would remain a degenerated problem. Other methods to observe Ganymede's atmosphere  
582 are therefore highly needed to resolve this non-constrained issue.

583

584 **Acknowledgement:** F.L., R.M. and J.-Y.C. acknowledge the support by ANR of the TEMPETE project  
585 (grant ANR-17-CE31-0016). Authors are also indebted to the "Système Solaire" and "Soleil  
586 Héliosphère et Magnétosphère" programs of the French Space Agency CNES for their supports. Work  
587 at Imperial College London was supported by the STFC of the UK under grant ST/W001071/1.  
588 Authors also acknowledge the support of the IPSL data center CICALAD for providing us access to their  
589 computing resources and data. Data may be obtained upon request from F. Leblanc  
590 (email:francois.leblanc@latmos.ipsl.fr).

591

592

593 **References**

594 Ajello J.M., Kanik I., Ahmed S.M. and J.T. Clarke, Line profile of H Lyman  $\alpha$  from dissociative excitation  
595 of H<sub>2</sub> with application to Jupiter, *J. Geophys. Res.* et al., 100, E12, 26411-26420, 1995

596 Alday J., L. Roth, N. Ivchenko, K. D. Retherford, T. M. Becker, P. Molyneux, and J. Saur. New constraints  
597 on Ganymede's hydrogen corona: Analysis of Lyman- $\alpha$  emissions observed by HST/STIS between 1998  
598 and 2014. *Planet. Space Sci.*, 148:35-44, Nov 2017. doi: 10.1016/j.pss.2017.10.006.

599 Barth, C.A., Hord, C.W., Stewart, A.I.F., Pryor, W.R., Simmons, K.E., McClintock, W.E., Ajello, J.M.,  
600 Naviaux, K.L. and Aiello, J.J.: Galileo ultraviolet spectrometer observations of atomic hydrogen in the  
601 atmosphere of Ganymede, *Geophys. Res. Lett.*, 24, 2147–2150, 1997

602 Broadfoot A. L., Belton M. J., Takacs P. Z., Sandel B. R., Shemansky D. E., Holberg J. B., Ajello J. M., Moos  
603 H. W., Atreya S. K., Donahue T. M., Bertaux J. L., Blamont J. E., Strobel D. F., McConnell J. C., Goody R.,  
604 Dalgarno A., and McElroy M. B. Extreme ultraviolet observations from Voyager 1 encounter with  
605 Jupiter. *Science*, 204:979–982, June 1979. doi: 10.1126/science.204.4396.979. URL  
606 <http://adsabs.harvard.edu/abs/1979Sci...204..979B>.

607 Buccino D.R., Parisi M., Gramigna E., Gomez-Casajus L., Tortora P., Zannoni M., Caruso A., Park R.S.,  
608 Withers P., Steffess P., Hodges A., Levin S. and Bolton S., Ganymede's Ionosphere observed by a Dual-  
609 Frequency Radio Occultation with Juno, *Geophys. Res. Let*, 2022. doi: 10.1029/2022GL098420.

610 Carnielli G., Galand M. Leblanc F., L. Leclercq, Modolo R. and A. Beth, First 3D test particle  
611 model of Ganymede's ionosphere, *Icarus*, 330, 42, 2019. <10.1016/j.icarus.2019.04.016> - insu-  
612 02111422

613 Carnielli G., M. Galand, F. Leblanc, R. Modolo, A. Beth, X. Jia, Constraining Ganymede's neutral and  
614 plasma environments through simulations of its ionosphere and Galileo observations, *Icarus*, 343,  
615 113691, 2020a. <10.1016/j.icarus.2020.113691>



616 Carnielli G., M. Galand, F. Leblanc, R. Modolo, A. Beth, X. Jia, Simulations of ion sputtering at  
617 Ganymede, *Icarus*, *Icarus*, 351, 113918, 2020b. <10.1016/j.icarus.2020.113918>

618 Cassidy T.A., C.P. Paranicas, J.H. Shirley, J.B. Dalton III, B.D. Teolis, R.E. Johnson, L. Kamp, A.R. Hendrix,  
619 Magnetospheric ion sputtering and water ice grain size at Europa. *Planet. Space Sci.* **77**, 64–73 (2013).  
620 <https://doi.org/10.1016/j.pss.2012.07.008>

621 Cooper J.F., R. E. Johnson, B. H. Mauk, H. B. Garrett, and N. Gehrels. Energetic Ion and Electron  
622 Irradiation of the Icy Galilean Satellites. *Icarus*, 149(1):133-159, 2001. doi: 10.1006/icar.2000.6498.

623 Dalgarno A., Yan M., W. Liu, Electron energy deposition in a gas mixture of atomic and molecular  
624 hydrogen and helium, *ApJS*, 125:237-256, 1999. 10.1086/313267

625 de Kleer K., Milby Z., Schmidt C., Camarca M. and M. Brown, The Optical Aurorae of Europa, Ganymede  
626 and Callisto, *The Planetary Science Journal*, 4:37, 2023. <https://doi.org/10.3847/PSJ/acb53c>

627 Feldman, P.D., McGrath, M.A., Strobel, D.F., Warren Moos, H., Retherford, K.D., Wolven, B.C., HST/STIS  
628 ultraviolet imaging of polar aurora on Ganymede. *Astrophys. J.* 535, 1085–1090, 2000.

629 Fray, N., Schmitt, B., Sublimation of ices of astrophysical interest: A bibliographic review. *Planet. Space*  
630 *Sci.* 57, 2053–2080, <http://dx.doi.org/10.1016/j.pss.2009.09.011>, 2009.

631 Hall, D.T., Feldman, P.D., McGrath, M.A., Strobel, D.F., The far-ultraviolet oxygen airglow of Europa and  
632 Ganymede, *The Astrophysical Journal* 499, 475, 1998.

633 Jia, X., Walker, R.J., Kivelson, M.G., Khurana, K.K., Linker, J.A., 2009. Properties of Ganymede’s  
634 magnetosphere inferred from improved three-dimensional MHD simulations. *Journal of Geophysical*  
635 *Research (Space Physics)* 114, A09209. URL: <http://adsabs.harvard.edu/abs/2009JGRA..114.9209J>,  
636 doi:<https://doi.org/10.1029/2009JA014375>.

637 Johnson P.V., J.W. McConkey, S.S. Tayal, and I. Kanik, Collisions of electrons with atomic oxygen:  
638 current status, *Can. J. Phys.* 83: 589–616, 2005, doi: 10.1139/P05-034

639 Johnson, R.E., Carlson, R.W., Cooper, J.F., Paranicas, C., Moore, M.H., Wong, M.C., 2004. In: Bagenal,  
640 F., Dowling, T., McKinnon, W. (Eds.), Jupiter Atmosphere, Satellites and Magnetosphere. Cambridge  
641 Univ. Press, Cambridge, UK, pp. 485–512.

642 Johnson, R.E., A.V. Oza, F. Leblanc, C. Schmidt, T.A. Nordheim, The Origin and Fate of O<sub>2</sub> in Europa's  
643 Ice: an Atmospheric Perspective, *Space Science Review*, 215, 1, 2019. <10.1007/s11214-019-0582-1> -  
644 [insu-02020077](https://doi.org/10.1007/s11214-019-0582-1)

645 Kanik I., C. Noren, 489 O. P. Makarov, P. Vatti Palle, J. M. Ajello, and D. E. Shemansky. Electron impact  
646 dissociative excitation of O<sub>2</sub>: 2. Absolute emission cross sections of the OI(130.4 nm) and OI(135.6 nm)  
647 lines. *J. Geophys. Res.*, 108:5126, 2003.

648 Leblanc F., Leclercq L., A. Oza, C. Schmidt, Modolo R., J.Y. Chaufray and R.E. Johnson, On the orbital  
649 variability of Ganymede's atmosphere *Icarus*, 293, 185-198, doi: 10.1016/j.icarus.2017.04.025, 2017.

650 Makarov, O. P., J. M. Ajello, P. Vattipalle, I. Kanik, M. C. Festou, and A. Bhardwaj, Kinetic energy  
651 distributions and line profile measurements of dissociation products of water upon electron impact, *J.*  
652 *Geophys. Res.*, 109, A09303, doi:10.1029/2002JA009353, 2004

653 Marconi, M.L., A kinetic model of Ganymede's atmosphere. *Icarus* 190, 155– 174, 2007.

654 Marzok, A., Schlegel, S., Saur, J., Roth, L., Grodent, D., Strobel, D. F., & Retherford, K. D. (2022).  
655 Mapping the brightness of Ganymede's ultraviolet aurora using Hubble Space Telescope observations.  
656 *Journal of Geophysical Research: Planets*, 127, e2022JE007256.  
657 <https://doi.org/10.1029/2022JE007256>

658 McClintock W. E., G. J. Rottman, and T. N. Woods. Solar-Stellar Irradiance Comparison Experiment II  
659 (Solstice II): Instrument Concept and Design. *Sol. Phys.*, 230:225-258, 2005.

660 McGrath, M.A., Xianzhe, J., Retherford, K., Feldman, P.D., Stroberl, D.F., Saur, J., Aurora on Ganymede.  
661 *J. Geophys. Res.: Space Phys.* 118 (5), 2043–2054, 2013.

662 Modolo R., S. Hess, M. Mancini, F. Leblanc, JY Chaufray, D. Brain, L. Leclercq, G. Chanteur, P. Weill,  
663 Gonzalez-Galindo, F. Forget, M. Yagi and C. Mazelle, Mars-solar wind interaction: LatHyS, an improved  
664 parallel 3D multi-species hybrid model, *J. Geophys. Res.*, 121 (7), 6378-6399, 2016.

665 Molyneux P. M., J. D. Nichols, N. P. Bannister, E. J. Bunce, J. T. Clarke, S. W. H. Cowley, J. C. Gérard, D.  
666 Grodent, S. E. Milan, and C. Paty. Hubble Space Telescope Observations of Variations in Ganymede's  
667 Oxygen Atmosphere and Aurora. *Journal of Geophysical Research (Space Physics)*, 123(5):3777-3793,  
668 2018. doi: 10.1029/2018JA025243.

669 Musacchio, F., J. Saur, L. Roth, K. D. Retherford, M. A. McGrath, P. D. Feldman, and D. F. Strobel (2017),  
670 Morphology of Ganymede's FUV auroral ovals, *J. Geophys. Res. Space Physics*, 122, 2855–2876,  
671 doi:10.1002/2016JA023220.

672 Neubauer, F.M., The sub-Alfvénic interaction of the Galilean satellites with the Jovian magnetosphere.  
673 *Journal of Geophysical Research* 104 (E2), 3863, 1999. <http://doi.wiley.com/10.1029/1998JE900031>

674 Oren M. and Nayar S. K., Generalization of Lambert's Reflectance Model, *Proceedings of the 21st*  
675 *Annual Conference on Computer Graphics and Interactive Techniques*: 239–246, 1994.  
676 [doi:10.1145/192161.192213](https://doi.org/10.1145/192161.192213)

677 Oza A. V., F. Leblanc, R. E. Johnson, C. Schmidt, L. Leclercq, Cassidy T. and J.Y. Chaufray, Dusk over dawn  
678 O<sub>2</sub> asymmetry in Europa's near-surface atmosphere, *Planetary & Space Science*, 167, 23-32, 2019.  
679 [doi.org/10.1016/j.pss.2019.01.006](https://doi.org/10.1016/j.pss.2019.01.006)

680 Plainaki, C., Milillo, A. , Massetti, S. , Mura, A., Jia, X., Orsini, S., Mangano, V., DeAngelis, E., Rispoli, R.,  
681 The H<sub>2</sub>O and O<sub>2</sub> exospheres of Ganymede: the result of a complex interaction between the jovian  
682 magnetospheric ions and the icy moon, *Icarus*, 245, 306–319,  
683 <http://dx.doi.org/10.1016/j.icarus.2014.09.018>, 2015.

684 Plainaki C., G. Sindoni, D. Grassi, L. Cafarelli, E. D'Aversa, S. Massetti, A. Mura, A. Milillo, G. Filacchione,  
685 G. Piccioni, Y. Langevin, F. Poulet, F. Tosi, A. Migliorini, and F. Altieri. Preliminary estimation of the

686 detection possibilities of Ganymede's water vapor environment with MAJIS. *Planet. Space Sci.*,  
687 191:105004, 2020a, doi: 10.1016/j.pss.2020.105004.

688 Plainaki C., S. Massetti, X. Jia, A. Mura, A. Milillo, D. Grassi, G. Sindoni, E. D'Aversa, and G. Filacchione.  
689 Kinetic Simulations of the Jovian Energetic Ion Circulation around Ganymede. *ApJ*, 900(1):74, 2020a.  
690 doi: 10.3847/1538-4357/aba94c.

691 Roth L., J. Saur, K. D. Retherford, P. D. Feldman, and D. F. Strobel. A phenomenological model of Io's  
692 UV aurora based on HST/STIS observations. *Icarus*, 228:386-406, 2014.

693 Roth L., J. Saur, K. D. Retherford, D. F. Strobel, P. D. Feldman, M. A. McGrath, J. R. Spencer, A. Blöcker,  
694 and N. Ivchenko. Europa's far ultraviolet oxygen aurora from a comprehensive set of HST observations.  
695 *Journal of Geophysical Research (Space Physics)*, 121:2143-2170, March 2016.

696 Roth L. et al., Evidence for a sublimated water atmosphere on Ganymede from Hubble Space Telescope  
697 Observations, *Nature*, 2021

698 Roth L., C. Plainaki, A.V. Oza, A. Vorburger, R.E. Johnson, P.M. Moyneux, K.D. Retherford, F. Leblanc, S.  
699 Massetti, A. Mura and P. Wurz, Ganymede's tenuous atmosphere, *Ganymede book*, 2022

700 Roth L., Marchesini G., Becker T.M., Hoeijmakers H.J., Molyneux, P.M., Retherford K.D., Saur J.,  
701 Carberry Mogan S.R. and J.R. Szalay, Probing Ganymede's Atmosphere with HST Ly $\alpha$  Images in Transit  
702 of Jupiter, *The Planetary Science Journal*, 4:12, 2023. <https://doi.org/10.3847/PSJ/acaf7f>

703 Saur, J., Duling, S., Roth, L., Jia, X., Strobel, D. F., Feldman, P. D., et al. (2015). The search for a subsurface  
704 ocean in Ganymede with Hubble Space Telescope observations of its auroral ovals. *Journal of*  
705 *Geophysical Research: Space Physics*, 120(3), 1715–1737. <https://doi.org/10.1002/2014JA020778>

706 Shemansky D.E., Yung Y.L., Liu W., Yoshii J., Hansen C.J., Hendrix A.R. and L.W. Esposito, A new  
707 understanding of the Europa Atmosphere and limits on geophysical activity, *ApJ*, 797-84, 2014. doi:  
708 10.1088/0004-637X/797/2/84

709 Shematovich, V.I., Neutral Atmosphere Near the Icy Surface of Jupiter's Moon Ganymede, Solar System  
710 Research, 2016, 50, 4, 262–280, 2016.

711 Song M.Y., Hyuck C., Karwasz G.P., Kokoouline V., Nakamura Y., Tennyson J., Faure A., Mason N.J. and  
712 Y. Itikawa, J. Phys. Chem. Ref. Data 50, 023103 (2021). doi: 10.1063/5.0035315

713 Spencer, J.R., Icy Galilean satellite reflectance spectra: less ice on Ganymede and Callisto? Icarus 70,  
714 99–110, 1987.

715 Spencer J. R., L. A. Lebofsky, and M. V. Sykes. Systematic biases in radiometric diameter  
716 determinations. Icarus, 78(2):337{354, 1989. doi: 10.1016/0019-1035(89)90182-6.

717 Stern, S.A., The lunar atmosphere: history, status, current problems and context, Reviews of  
718 Geophysics, 37, 4, 453–491, 1999.

719 Tayal S.S. and O. Zatsarinny, *B-spline R-matrix-with-pseudostates* approach for excitation and  
720 ionization of atomic oxygen by electron collisions, Physical Review A 94, 042707, 2016. doi:  
721 10.1103/PhysRevA.94.042707

722 Turc, L., Leclercq, L., Leblanc, F., Modolo, R., Chaufray, J.-Y., Modelling Ganymede's neutral  
723 environment: A 3D test-particle simulation. Icarus 229, 157–169, 2014.

724 Vasyliūnas V.M. and A. Eviatar, Outflow of ions from Ganymede: a reinterpretation, Geophys. Res. Let.,  
725 27, 9, 1347-1349, 2000.

726 Vorburger A., Fatemi S., Galli A., Liuzzo L., Poppe A.R. and P. Wurz, 3D Monte-Carlo simulation of  
727 Ganymede's water exosphere, Icarus, 375, 114810, 2022.  
728 <https://doi.org/10.1016/j.icarus.2021.114810>